Available online at www.sciencedirect.com
SCIENCE DIRECT®
ELSEVIER
Nuclear Instruments and Methods in Physics Research A 551 (2005) 88–107
NUCLEAR INSTRUMENTS & METHODS IN PHYSICS RESEARCH Section A
www.elsevier.com/locate/nima

Results on disordered materials from the GEneral Materials diffractometer, GEM, at ISIS ☆

Alex C. Hannon*

ISIS Facility, Rutherford Appleton Laboratory, Chilton, Didcot, Oxon OX11 0QX, UK

Available online 15 August 2005

Abstract

The GEneral Materials diffractometer, GEM, at the ISIS Facility pulsed neutron source is the most advanced materials neutron diffractometer in the world. A full description of GEM is given from the point of view of structural studies of disordered materials. The key component for these studies is the highly stable detector array, which covers a very wide range in scattering angles and a very large solid angle, leading to a wide dynamic range and a high count rate. The high real-space resolution of GEM, due to a high maximum momentum transfer of 55 $Å^{-1}$, is illustrated by data on bioactive phosphate glasses, where bonds from phosphorus to bridging and non-bridging oxygens (which differ in length by approximately 0.12 Å) are clearly resolved. The low momentum transfer ability of GEM is demonstrated by a measurement on amorphous $Si_{77}D_{23}$, which yields reliable data down to 0.1 $Å^{-1}$. The first successful isotopic substitution experiment on sol–gel materials has been performed on GEM in a study of amorphous titanium silicates, showing the suitability of the instrument for both isotopic substitution, and for studies of complex materials, even in the presence of hydrogen. Studies of the structures of disordered group 11 cyanide crystals show the power of GEM to reveal the nature of disorder in crystalline systems as well as glassy materials. The crystal structure of high temperature CuCN has been solved for the first time. The disorder in AuCN, AgCN and high temperature CuCN arises from random displacements of the linear –M–(C≡N)– chains relative to each other, and the one-dimensional negative thermal expansion is due to long wavelength cooperative motions of the chains.
© 2005 Elsevier B.V. All rights reserved.

PACS: 61.12.Ex; 61.43.−j; 61.43.Fs

Keywords: Neutron diffraction; Instrumentation; Glass; Amorphous; Disorder; Sol–gel

1. Introduction

The GEneral Materials diffractometer, GEM, at the ISIS Facility pulsed neutron source is the world's most advanced materials neutron diffractometer [1,2]. Of great importance to the success of

☆Paper presented at the Fall Meeting of the European Materials Research Society, Warsaw, 5–10 September, 2004, in Symposium D, "Applications of Linear and Area Detectors for X-ray and Neutron Diffraction and Spectroscopy".

*Tel.: +44 1235 445358; fax: +44 1235 445720.
E-mail address: a.c.hannon@rl.ac.uk.

0168-9002/$ - see front matter © 2005 Elsevier B.V. All rights reserved.
doi:10.1016/j.nima.2005.07.053

GEM has been the detector array, which covers a very large area and a wide range in scattering angles, and gives data with a high stability and high resolution. GEM is of great use for a wide variety of studies of ordered crystalline materials, and these are discussed elsewhere [3–6]. This paper describes, and illustrates by examples, the performance of GEM for structural studies of disordered materials. The ability of GEM to measure data up to high momentum transfers, giving good real-space resolution, is illustrated by data on phosphate glasses. Data on amorphous silicon are used to demonstrate the ability of GEM to measure data at low momentum transfers, extending into the small angle neutron scattering (SANS) region. The advantages of GEM for difference experiments, due to its high count rate and stable detectors, are illustrated by isotopic substitution measurements for titanium in mixed titania–silica sol–gel materials. Finally, results on disordered cyanide crystals are described as an example of the high suitability of GEM for studies of the structure of disordered crystalline materials.

A comprehensive review of the studies of disordered materials that have been performed on GEM is beyond the scope of this paper; besides the work described here, there have also been studies of the structure of alkali-ammonia solutions [7], tellurite glasses [8–10], phosphate glasses [11–13], vanadate glasses [14], oxycarbide and carbonitride glasses [15–17], amorphous zeolite precursors [18], paracrystalline carbons [19] and carbon nanotubes [20,21]. GEM has also made an impact on the investigation of the structure of disordered crystals, such as a study of the local atomic strain in alloys [22], and crystals of mineralogical interest, such as the phases of silica [23–25] and related piezoelectric materials [26]. The high count rate of GEM also makes it well suited to the study of dynamic processes, such as the crystallisation of glasses and amorphous metals [27,28].

2. Outline of theory

The quantity measured in a neutron diffraction experiment [2,29] is the differential cross-section

$$\frac{d\sigma}{d\Omega} = I^S(Q) + i(Q) \tag{1}$$

where $\hbar Q$ ($= 4\hbar\pi \sin\theta/\lambda$) is the magnitude of the momentum transfer, $I^S(Q)$ is the self-scattering and $i(Q)$ is the distinct scattering. The self-scattering, which is subtracted from the data to give the distinct scattering, may be calculated approximately [30–32] according to

$$I^S(Q) = \sum_l c_l \overline{b_l^2}(1 - P_l(\theta, \mu_l, \bar{K}, f, \varepsilon(E), \phi(E))) \tag{2}$$

where the Placzek [33] inelasticity correction for pulsed neutron diffraction, P_l, depends upon the scattering angle 2θ, the ratio, μ_l, of the atomic mass of atom l to that of the neutron, the average kinetic energy, $\bar{K}$, per atom (which depends on the sample temperature), the ratio, $f = L_2/(L_1 + L_2)$, of scattered-to-total flight path, the energy dependent detector efficiency, $\varepsilon(E)$, and the energy-dependent incident neutron flux $\phi(E)$. The l summation is performed over the N elements in the sample, and c_l and $4\pi\overline{b_l^2}$ are, respectively, the atomic fraction and the total neutron scattering cross-section of element l. Structural information may be obtained by using a Fourier transform to obtain the total correlation function

$$T(r) = T^0(r) + \frac{2}{\pi}\int_0^\infty Qi(Q)M(Q)\sin(rQ)\,dQ \tag{3}$$

where $M(Q)$ is a modification function, introduced to take into account the maximum experimentally attainable momentum transfer, Q_{max}. The average density contribution to $T(r)$ is

$$T^0(r) = 4\pi r g^0 \left(\sum_l c_l \bar{b}_l\right)^2 \tag{4}$$

in which the l summation is performed over the N elements in the sample, g^0 is the atomic number density, and c_l and $\bar{b}_l$ are, respectively, the atomic fraction and coherent scattering length for element l. The correlation function is a weighted sum of partial correlation functions, $t_{ll'}(r)$:

$$T(r) = \sum_{ll'} c_l \bar{b}_l \bar{b}_{l'} t_{ll'}(r) \tag{5}$$

where the l, l' summations are each over the elements of the sample.

The most straightforward modification function is the 'step' function which equals unity for $Q \leqslant Q_{\max}$ and is zero for $Q > Q_{\max}$. The step function (which is equivalent to using no modification function) yields the best real-space resolution, with a full-width at half-maximum (FWHM) $\Delta r_{\text{step}} = 3.791/Q_{\max}$, but at the expense of relatively large termination ripples on either side of a real peak in the correlation function, $T(r)$. The Lorch [34] modification function is very widely used, and this is defined as follows:

$$M_{\text{Lorch}}(Q) = \begin{cases} \frac{\sin(\Delta r Q)}{\Delta r Q} & Q \leqslant Q_{\max},\ \Delta r = \pi/Q_{\max} \\ 0 & Q > Q_{\max}. \end{cases} \tag{6}$$

The use of the Lorch function reduces the termination ripples to a very large extent. Indeed with the high $Q_{\max}$ of pulsed neutron diffraction, the effect of thermal motion is often to entirely remove the termination ripples from the correlation function. However, this gain is realised at the expense of some loss of resolution, with a FWHM $\Delta r_{\text{Lorch}} = 5.437/Q_{\max}$.

3. The GEM diffractometer

The GEM diffractometer was designed to be at the forefront of what can currently be achieved with a materials diffractometer on a pulsed neutron source. The most important component in achieving this has been the detector array, which has a very large area of 7.270 m^2 and a very wide range in scattering angles from 1.2° to 171.4°. The resolution in reciprocal-space is excellent, with a best value of $\Delta Q/Q = 0.34\%$ at backward angle. The detectors are extremely stable with a 0.1% variation in efficiency over a 24 h period.

GEM receives neutrons from a normal view of a liquid methane moderator at a temperature between 100 and 110 K, using a beam port which was previously used by the Liquids and Amorphous Diffractometer (LAD) [2,35]. LAD was a highly successful diffractometer, and to date the work performed on LAD has resulted in about 416 scientific publications (see Ref. [36] for example). LAD was the first ISIS instrument to be used for experiments, and the valuable experience during its 17 years of operation made it clear that a much more advanced materials diffractometer could be constructed.

The length of the primary flight path of GEM, from moderator to sample, L_1, is 17 m. This relatively long flight path (for LAD L_1 was 10 m) leads to a high resolution in reciprocal-space, especially at backward angle, by reducing the time-of-flight (t-o-f) and flight path contributions to the resolution [2]. Clearly, this high resolution is of great advantage to crystallography experiments, since it leads to a good separation of the Bragg peaks in a powder diffraction pattern. The high resolution is gained at the expense of a reduced incident flux (due to the long L_1) which is per se a disadvantage for studies of non-crystalline materials. Nevertheless, the high Q-resolution is advantageous for correlation function studies, since it leads to more accurate coordination numbers. This is because the effect of resolution broadening of the distinct scattering, $i(Q)$, is to progressively damp the differential correlation function, $D(r) = T(r) - T^0(r)$, which leads to a reduction in measured coordination numbers [37] and a distortion of the real-space peak shape [38]. Furthermore, the long primary flight path is advantageous for studies of disordered materials because it should lead to a reduction of the inelasticity correction [30–32], due to the reduction in the flight path ratio, f, which results in straighter integration paths in $Q-E$ space.

The primary flight path of GEM, shown in Fig. 1, is evacuated to prevent the attenuation of the beam by air scattering. There is a sequence of computer controlled horizontal and vertical slits (at distances of 6.352, 8.145, 10.265, 12.675 and 15.350 m from the moderator) made of sintered boron carbide, which allow the dimensions of the beam to be accurately defined. There are two disc choppers in the primary flight path, at distances of 6.5 and 9.75 m from the moderator, which are used to prevent frame overlap problems. The disc chopper at 6.5 m has a variable opening aperture which is normally set to its widest setting of 112°. In normal operation the disc choppers define a

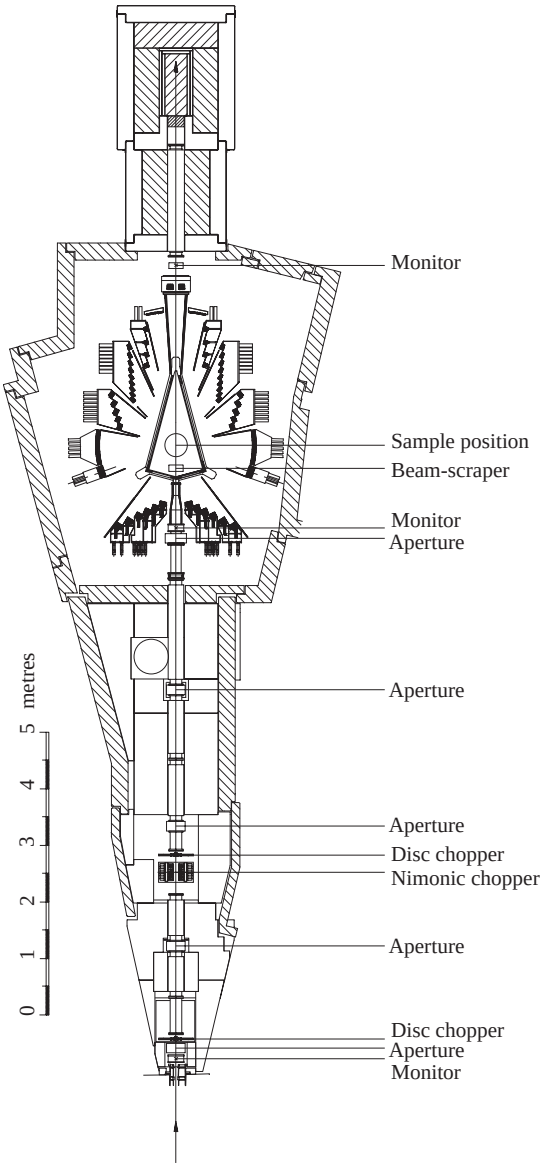

Fig. 1. The GEM beamline.

wavelength band from 0.05 to 3.40 Å. However, this band can be shifted to longer wavelengths so that the data cover a lower Q-range. There is also a 50 Hz nimonic chopper at 9.45 m from the moderator, whose purpose is to reduce backgrounds by removing the fast neutrons from each pulse. However, this chopper is not normally used for experiments on disordered materials because it does not move out of the beam sufficiently quickly and hence it curtails the minimum wavelength and thence the value of Q_{max}. There are four neutron beam monitors at distances of 6.22, 10.147, 15.535 and 20.145 m from the moderator, to measure the neutron flux. These are of a novel design, where a thin vanadium foil is located in the beam, and then shielded neutron detectors measure the scattering from the vanadium. This design ensures the monitor performs a uniform sampling across the profile of the beam.

As shown in Fig. 2, the sample on GEM is contained within an evacuated sample tank. The detectors are located outside the sample tank, and they view the sample through thin 0.7 mm windows made of aero grade aluminium. Prior to the sample position, at 16.550 m from the moderator, is a beam-scraper. The beam-scraper is a final computer controlled aperture, whose purpose is to precisely define the dimensions of the beam which is incident on the sample.

The sample tank contains an oscillating radial collimator (ORC) which collimates the secondary flight path, thus reducing the background [39]. The blades of the ORC are 10 cm wide, and made of 0.2 mm mylar, coated on both sides with a large number of layers of ^{10}B paint. The inner edge of each blade is 20 cm from the sample position, and the blades cover scattering angles from 6° to 170° (when the ORC is stationary), with an angular spacing between the blades of 2°. The oscillating mechanism for the ORC is driven by a stepper motor and a novel electronics system has been developed to control it. Over most of its range of movement the ORC moves at a constant angular velocity, but at the end of each movement there is a short time of very rapid deceleration and acceleration. During this short time the acquisition of neutron counting data is suspended, and in this way it is ensured that data are collected with a uniform angular masking of the detectors by the ORC blades.

The detectors on GEM are all ZnS/^{6}Li scintillator detectors, and the principles of operation of the GEM detector system is dealt with in detail elsewhere [40]. Each detector element is composed of two strips of scintillator material, arranged in a V-shape. The tip of the V-shape is directed towards the sample, so that a neutron has a long

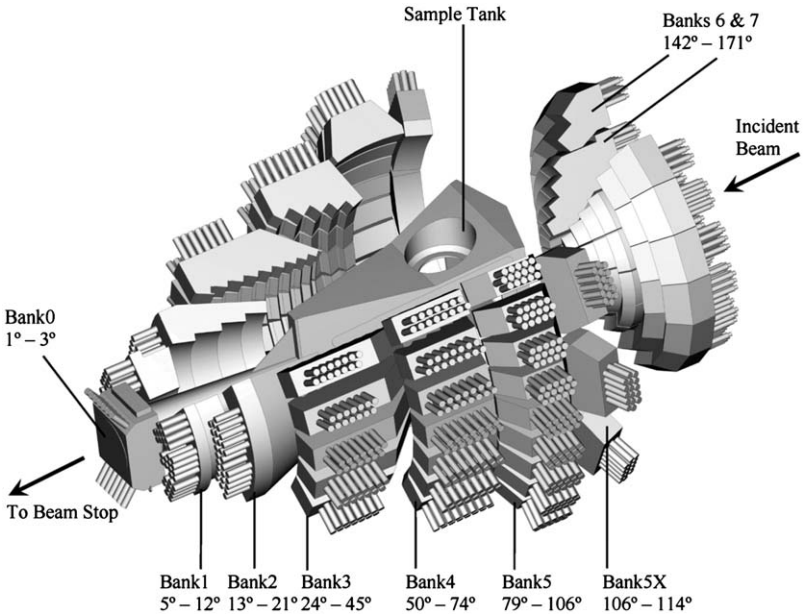

Fig. 2. A schematic layout of the detector banks of the GEM detector array.

path through the scintillator, and yet the distance for the scintillation light to get out of the scintillator is short. Most of the detector elements are 200 mm long, with an effective width of 5 mm. This relatively narrow width is an important factor in determining the excellent resolution in reciprocal-space. The absorption of a neutron in a detector element results in a flash of light which is transmitted via fibre optic cables to photomultiplier tubes (PMTs). Each element is connected to two PMTs, and a coincidence system is used, so that the number of PMTs is less than the number of elements by an overall factor of approximately six. An important aspect of the GEM project was the development of high stability detectors. A variation of the detector efficiency with temperature of 0.12% per degree has been achieved by means of a redesign of the ISIS signal electronics mounted on each PMT [40]. In order to minimise the effects of stray magnetic fields, each PMT is individually housed in a mu-metal shield and a low carbon steel tube.

The detector elements are grouped together in modules which contain typically about 100 parallel elements. The modules are arranged so that each element is tangential to a Debye–Scherrer cone of diffraction, with the two ends of the element equidistant from the sample. The detector modules are arranged in banks which cover a limited range in scattering angle. The elements within a bank are arranged so that they are approximately on a path of constant resolution (i.e. they are approximately resolution focused).

There are eight detector banks on GEM and their parameters are given in Table 1. The very wide range in scattering angle, 2θ, of the GEM detector system leads to a very wide range in $Q(=4\pi\sin\ \theta/\lambda)$ for the final result. This is advantageous for studies of disordered materials which, as will be discussed later, require that the results extend both as close to zero Q as possible, and to as high a $Q_{\max}$ as possible. Neutron scattering is an intensity limited technique, and this is especially significant for non-crystalline diffraction, where the intensity is distributed relatively evenly in Q, rather than being concentrated in intense Bragg peaks. It is thus very important to attain as high a count rate as possible, and on GEM this has been achieved by having a very large number of detectors, so that

Table 1
Parameters of the GEM detector array

Detector Bank	Scattering angle 2θ (deg)	Range in azimuthal angle ϕ (deg)	Secondary flight path L_2 (m)	Number of detector elements/ modules	Solid angle Ω (sr)	Resolution $\Delta Q/Q$(%)	Minimum accessible momentum transfer Q_{min} (Å^{-1})
Bank0	1.21–3.18	± 90.0	2.757–2.767	80/4	0.008	5–10	0.04
Bank1	5.32–12.67	± 45.0	2.365–2.376	330/6	0.056	4.7	0.17
Bank2	13.44–21.59	± 43.4	1.477–2.100	320/4	0.093	2.4	0.43
Bank3	24.67–45.61	± 42.5	1.077–1.893	900/10	0.478	1.7	0.79
Bank4	50.07–74.71	± 44.4	1.028–1.436	1400/14	0.988	0.79	1.56
Bank5	79.07–106.60	± 44.5	1.376–1.383	2160/18	1.135	0.51	2.35
Bank5X	106.02–114.19	± 42.7	1.377–1.387	720/18	0.378	0.5	2.95
Bank6	142.50–149.72	± 69.3	1.544–1.738	560/14	0.280	0.34	3.50
Bank7	149.98–171.40	± 66.6	1.035–1.389	800/10	0.443	0.35	3.57

there is a very large detector area and solid angle. In order to obtain this large detector solid angle, the detectors cover a wide range in azimuthal angle, ϕ (mostly $\pm 45°$). This is to be contrasted with early diffractometers, such as LAD [2,35], where the detectors were located only in the equatorial plane. The total solid angle of the GEM detector array is 3.860 steradians, and the detectors cover more than 30% of all possible scattering directions from the sample.

Of particular note is Bank0, the lowest angle detector bank. Unlike all the other detectors, Bank0 is located inside the vacuum system, in the get-lost tube. There were significant technical challenges to operating this detector bank under vacuum, but these were successfully overcome, as demonstrated by the results shown in Section 5.

The minimum accessible momentum transfer, Q_{min}, given in Table 1, is calculated on the assumption that the standard wavelength range of GEM is used. In practice the minimum useful momentum transfer is higher than the values given, because the data become unreliable at the extreme long wavelength limit, due to a combination of experimental effects (background, absorption, inelasticity). The maximum useful momentum transfer, Q_{max}, depends primarily upon the damping rate of the information in the distinct scattering, $i(Q)$, of the sample, due to static and thermal disorder. Most of the GEM detector banks yield data up to maximum momentum transfers in excess of 100 Å^{-1}, but even for a well-ordered sample, such as the phosphate glasses described in Section 4, oscillations in the distinct scattering cannot be discerned above about 50–60 Å^{-1}, due to the effective Debye–Waller factor, $\exp(-2W)$, which results from static and thermal disorder.

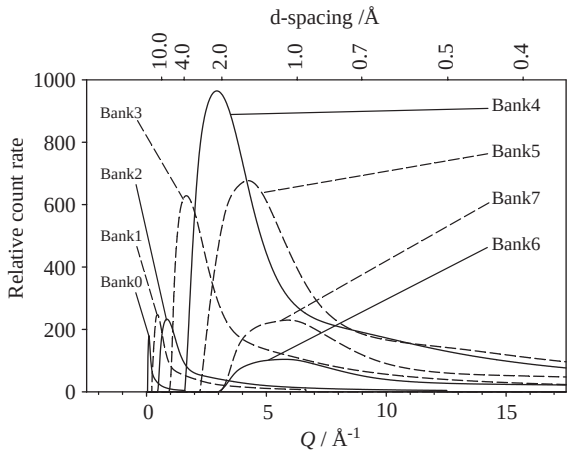

Fig. 3. The relative count rates of the GEM detector banks as a function of Q, and d-spacing. The odd numbered banks are shown using dashed lines, whilst continuous lines are used for the even numbered banks.

Fig. 3 shows the relative count rates per inverse Ångstrom of the GEM detector banks (not including Bank5X). The data for this figure were produced by measuring the scattering from a

standard 6 mm diameter rod of vanadium, since the scattering from vanadium is almost entirely incoherent. The data in the figure have been subjected to a smoothing process, in order to remove the small residual vanadium Bragg peaks. The broad peak in these count rate curves arises from the moderator Maxwellian, and generally its position moves to higher Q as 2θ increases. Over most of the significant Q-range for non-crystalline diffraction, the highest count rate comes from Bank4 and Bank5; this is because the greatest solid angle is available at a scattering angle, 2θ, of 90°. As Fig. 3 shows, Bank5 gives the highest count rate in the high Q region (above about 11 Å^{-1}), which is very important for the study of disordered materials (see Section 4). This is to be contrasted with the situation for first generation disordered materials diffractometers, such as LAD [2,35], for which the high Q part of the diffraction pattern was derived from backward angle detectors at scattering angles of about 150°. As Johnson et al. [41] have shown, backward angle detectors should not be used in the derivation of the distinct scattering, $i(Q)$, if significant static approximation distortions of the data are to be avoided. Thus, GEM provides a qualitative improvement in the data, compared to LAD, in addition to the gain in count rate.

The count rate of GEM is high because of the large number of detector elements (7270), but the count rate of an individual detector element is low. Typically, a GEM detector element counts less than one neutron per 20 ms ISIS frame. The peak count rate, at short t-o-f, for a detector element is less than 100 Hz (i.e. mean time between counts $\tau_{\text{element}} \sim 10{,}000\,\mu\text{s}$) and the peak count rate for a module is less than 10,000 Hz ($\tau_{\text{module}} \sim 100\,\mu\text{s}$). The sustainable dead-time for an element is estimated at 10 μs, whilst the dead-time for the encoder for a module is estimated at 2 μs, and therefore dead-times in the GEM detector system only have a very slight effect.

The construction of GEM was a major undertaking, starting in 1999, and is only now nearing completion. An important factor in keeping the cost and timescale for detector manufacture to acceptably low levels involved training companies outside the laboratory to construct the scintillator modules. The 90° detectors, Bank5, have proved so successful that an extension to this bank, Bank5X, was recently installed. The final stage in the construction of GEM will be the installation of a lifting mechanism which will enable the ORC to be withdrawn from use when not required.

4. High Q study of phosphate glass structure

This section describes some measurements on phosphate glasses which illustrate how, in favourable cases, the high count rate of Bank5 makes it possible to measure reliable and useful data up to high maximum momentum transfers, Q_{max}, yielding excellent resolution in real-space. There is currently considerable interest in these bioactive glasses for medical use as both bone and dental implants [42,43]. In this paper only the phosphorus–oxygen bonds will be analysed in detail, and a full consideration of the glass structure may be found elsewhere [44,45].

Three samples of metaphosphate composition (i.e. 50 mol% P_2O_5) were studied; these were of composition $2AO \cdot Na_2O \cdot 3(P_2O_5)$ where A is Ca, Ba or Sr (these samples are referred to in Table 2 as Ca33, Ba and Sr). Two more calcium-containing samples with 45 mol% P_2O_5 were studied, of compositions $35CaO \cdot 20Na_2O \cdot 45P_2O_5$ and $40CaO \cdot 15Na_2O \cdot 45P_2O_5$ (referred to in Table 2 as Ca35 and Ca40). The samples were in the form of solid glass rods of diameter 0.8 cm and height 4.85 cm. Because the samples were in this form it was not necessary to use a container, such as a vanadium can, and hence excellent data corrections and normalisation were achieved. No Bragg peaks (which might arise from crystalline impurities in the samples) were observed. The level of the observed scattering agreed with the calculated scattering to within 2% or less and hence it is concluded that there is negligible H_2O or –OH in the samples, since even a small amount of hydrogen would lead to a large additional incoherent signal. The data collection time was typically about 8 h for each sample.

Oscillations were apparent in the data up to a maximum momentum transfer, Q_{max}, of 55 Å^{-1}, although the data for the Sr-containing sample

Table 2
Results from fitting the two components of the first P–O peak of the phosphate glass correlation functions, obtained using no modification function

Sample	Ba	Sr	Ca33	Ca35	Ca40
N_O/N_P	3.0	3.0	3.0	3.111	3.111
$r_{P\text{-}NBO}$ (Å)	1.4796(5)	1.4801(9)	1.4800(6)	1.4893	1.4891
$\langle u^2_{P\text{-}NBO}\rangle^{1/2}$ (Å)	0.0343(5)	0.0346(9)	0.0362(5)	0.0364(5)	0.0374(6)
$n_{P\text{-}NBO}$	1.83(3)	1.85(5)	1.87(3)	2.10(3)	2.11(3)
$r_{P\text{-}BO}$ (Å)	1.6018(9)	1.6001(16)	1.5977(10)	1.6028(11)	1.6006(12)
$\langle u^2_{P\text{-}NBO}\rangle^{1/2}$ (Å)	0.0497(9)	0.0497(14)	0.0490(9)	0.0490(−)	0.0490(−)
$n_{P\text{-}BO}$	1.99(3)	2.01(5)	1.96(4)	1.75(2)	1.72(3)
Total n_{P-O} ($=n_{P\text{-}NBO}+n_{P\text{-}BO}$)	3.82(6)	3.85(10)	3.83(7)	3.85(5)	3.83(6)

Statistical errors from the fits are given in brackets.

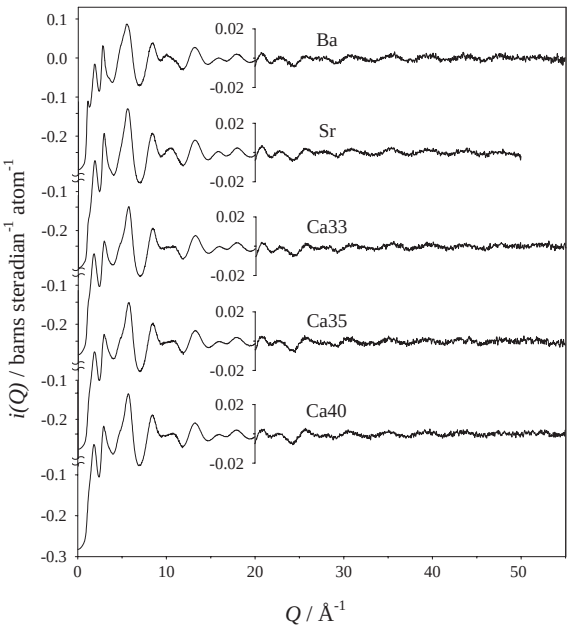

Fig. 4. The distinct scattering, $i(Q)$, for the phosphate glass samples, Ba, Sr, Ca33, Ca35, Ca40 (from top to bottom; see text for sample compositions).

could not be used above 50 $Å^{-1}$ due to the nuclear resonance of ^{87}Sr at 3.54 eV [46]. The data were reduced and corrected for attenuation and multiple scattering using the gudrun program [47,48]. Gudrun is preferred for this purpose because it takes into account the azimuthal detector angle, which is an important consideration for GEM. The Placzek inelasticity correction and the merging of data from different detector banks was

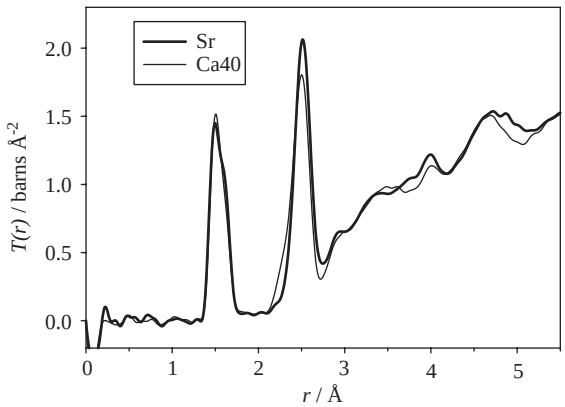

Fig. 5. The total correlation function for the Sr (thick line) and Ca40 (thin line) phosphate glass samples, calculated using the Lorch [34] modification function.

performed using the ATLAS suite of programs [49]. The distinct scattering for the samples is shown in Fig. 4, whilst the correlation functions are shown in Fig. 5 and Fig. 6. The first peak of the correlation functions at roughly 1.5 Å is due to P–O bonds, whilst the second peak at about 2.51 Å is due primarily to O–O correlations, but with smaller contributions due to Na–O, Ba–O, Sr–O and Ca–O. The first peak is split into two components, the first of which is due to bonds to non-bridging oxygens (NBOs—often called terminal oxygens in the phosphate glass field), whilst the second is due to bonds to bridging oxygens (BOs).

Initially, the data were Fourier transformed using the Lorch modification function [34], and

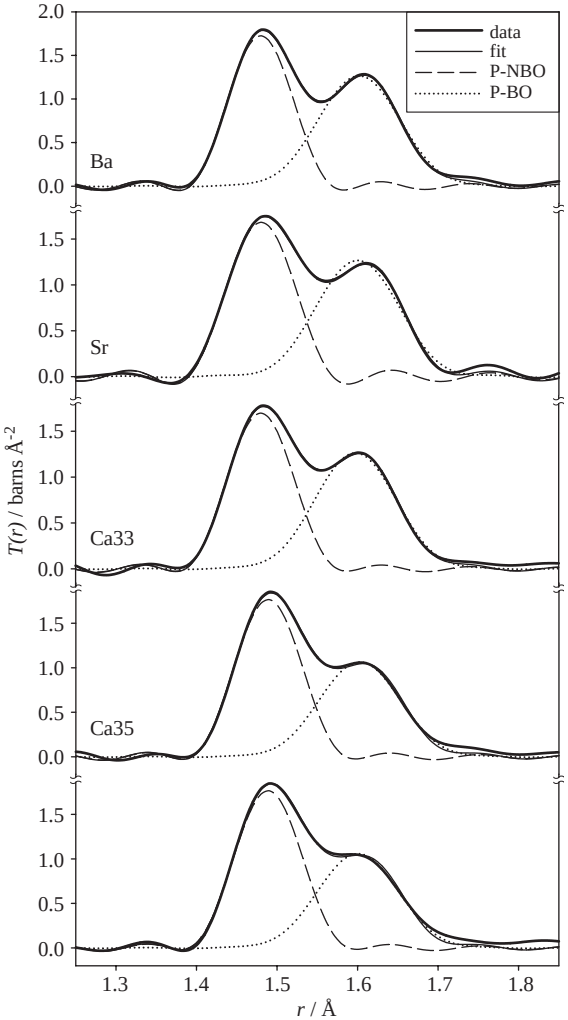

Fig. 6. The total correlation function calculated using no modification function and fitted in the first peak region, showing the data (thick line), fit (thin line) and P-NBO (dashed line) and P-BO components (dotted line) of the fit.

then the first peak region of the correlation function, $T(r)$, was fitted by the sum of two peaks. Although the total P–O coordination number was found to be close to four, as is expected for these tetrahedral glasses, the two contributing coordination numbers ($n_{\text{P-NBO}}$ and $n_{\text{P-BO}}$) were not consistent with expectation. This is because the two contributions to the first peak were not sufficiently well resolved for a reliable fit to be achieved—instead the longer distance contribution tended to become too broad in the fit, gaining too much area and hence giving too high a coordination number. The contributing coordination numbers for the three metaphosphate samples did not show a high degree of consistency, and there was even more inconsistency for the contributing coordination numbers for the two samples with 45 mol% P_2O_5.

Finally, the data were Fourier transformed using no modification function (i.e. a step modification function), which yields a narrower real-space resolution. It was found that the two contributions to the first peak were then sufficiently well resolved for reasonable results to be obtained when fitting the correlation functions for the metaphosphate samples; the total P–O coordination number was close to four, and the two contributing coordination numbers were almost equal, as is expected at the metaphosphate composition (see below). For the two samples with 45 mol% P_2O_5 the contributing coordination numbers were still not reasonable; again the longer distance contribution became too wide. This is because the second contribution (P-BO) is smaller for these samples, than for the metaphosphate samples. However, it was noted that the width of the second contribution shows almost no variation in the results for the three metaphosphate samples. Hence, the correlation functions for the two samples with 45 mol% P_2O_5 were fitted with the root-mean-square (RMS) distance variation of the second contribution fixed at 0.049 Å. The coordination number results obtained using this approach were found to be satisfactory. $\langle u_{i-j}^2 \rangle^{1/2}$ represents the RMS variation in the interatomic distance r_{i-j} for atom pair i–j, according to the formalism given by Hannon et al. [50].

If it is assumed that all phosphorus atoms are coordinated by four oxygens, and that all oxygens are bonded to either one or two P, then the P-NBO coordination number is

$$n_{\text{P-NBO}} = 2\frac{N_{\text{O}}}{N_{\text{P}}} - 4 \tag{7}$$

and similarly the P-BO coordination number is

$$n_{\text{P-BO}} = 8 - 2\frac{N_{\text{O}}}{N_{\text{P}}}. \tag{8}$$

N_O and N_P are the relative numbers of oxygen and phosphorus atoms in the sample. Therefore the metaphosphate samples (Ba, Sr and Ca33) are predicted to have values of two for both of the contributing P–O coordination numbers. For the Ca35 and Ca40 samples, the predicted coordination numbers are $n_{P\text{-}NBO} = 2.222$ and $n_{P\text{-}BO} = 1.777$. Measured coordination numbers tend to be slightly below expected values, most likely due to the effects of reciprocal-space resolution [37]. Therefore, the measured P–O coordination numbers (both total n_{PO}, and the two contributions, $n_{P\text{-}NBO}$ and $n_{P\text{-}BO}$) are consistent with prediction. These results are consistent with the results of other studies of metaphosphate glasses in the literature [51,52].

5. SANS study of amorphous silicon

Ideally the Fourier transform of Eq. (3) should be performed using measured data extending down to a minimum momentum transfer, Q_{min}, of zero, but in practice this cannot be achieved. Instead the diffraction pattern must be measured to as low a value of Q_{min} as can be attained. More significantly, if Q_{min} is too high, then features in the diffraction pattern relating to order at longer length scales may be missed. The low Q region is important because it may contain SANS arising from ordered structures in the sample on length scales which are larger than interatomic separations, with dimensions in the range from about 10 Å to about 1000 Å. Windsor and Sinclair [53] have proposed that it is of great advantage for a materials diffractometer to be able to measure the SANS simultaneously with the conventional wide angle neutron scattering (WANS) region of the diffraction pattern. With its unique low angle Bank0, GEM has realised this proposal.

The minimum accessible momentum transfer for each GEM detector bank given in Table 1 has been determined from the standard wavelength range of the instrument. However, in practice the minimum useful momentum transfer for a detector bank on a t-o-f diffractometer is not determined by its wavelength range, but by the range over which its results are reliable, and not excessively affected by the experimental corrections. The reason for this is that most of the experimental corrections (background, absorption, inelasticity) for a t-o-f diffractometer [49] tend to become large at low Q. For example, a background component which is independent of t-o-f is proportional to $1/Q$ when the data are converted to a momentum transfer scale. The materials studied on GEM which give rise to SANS are usually of types which have a SANS signal that decreases monotonically with increasing Q. For example, the differential cross-section may follow the Porod law [54] so that it is proportional to Q^{-4}. Thus, if a signal is observed which rises as Q becomes small, then in practice it may be difficult to determine whether this is due to SANS or to the experimental effects for which the data must be corrected. Amorphous silicon was chosen to test the low Q abilities of Bank0 on GEM because, unusually, it gives rise to a peak in the SANS region [55], which is of considerable advantage in distinguishing between a genuine SANS signal and experimental artefacts.

Amorphous silicon is usually prepared by glow discharge decomposition of silane (SiH_4) gas, and contains a significant proportion of hydrogen. The sample studied on GEM was prepared from deuterated silane and was of composition $Si_{77}D_{23}$. Fig. 7 shows previous data [55] for this sample, measured on the former SANS instrument D17 at the Institut Laue Langevin, Grenoble, together with the data measured by Bank0 on GEM. The GEM data were not normalised

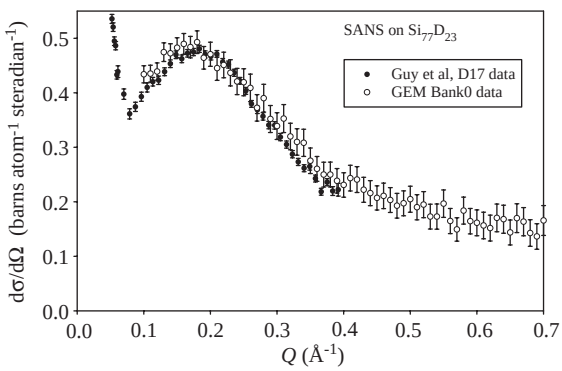

Fig. 7. The small angle neutron scattering signal for amorphous $Si_{77}D_{23}$, as measured by the D17 SANS instrument [55] (filled circles) and Bank0 on GEM (open circles).

absolutely, but instead were scaled to be consistent with the D17 data. The two data sets then agree well, confirming the ability of Bank0 to measure data into the SANS regime. In favourable cases, using the standard wavelength range of GEM, data can be measured reliably down to a Q_{min} of $0.1\,\text{Å}^{-1}$. If the frame overlap choppers are adjusted to give a shorter wavelength range, then even lower values of Q_{min} are accessible. The peak in the SANS signal has been found to be at $Q_p = 0.175 \pm 0.005\,\text{Å}^{-1}$ [55], and is associated with high pressure molecular hydrogen [56] trapped in the cages of the amorphous network, of mean radius $6.5 \pm 0.3\,\text{Å}$

6. Isotopic substitution on Ti in mixed titania–silica sol–gel glasses

This section describes the first successful isotopic substitution experiment to be performed on sol–gel materials [57,58]. These materials present relatively large difficulties for neutron diffraction, because of the ubiquitous presence of hydrogen (in the form of H_2O or –OH) in sol–gel samples. Hydrogen gives rise to difficulties as a result of its very large incoherent scattering cross-section, and the very large inelasticity effects associated with its low mass.

Isotopic substitution is the most common type of difference experiment to be performed by neutron diffraction—it involves extracting partial correlation information by performing subtractions between diffraction data sets. For difference experiments to work successfully, it is essential that the detector system has a high degree of stability, and the results on sol–gel glasses are an excellent demonstration of the suitability of GEM for this kind of measurement.

Titania–silica mixed oxide glasses, TiO_2–SiO_2, have received much recent attention as a result of their technologically useful physical properties. They are of use as ultra-low thermal expansion glasses [59] and as thin films with tailored refractive indices [60]. The greatest amount of recent work, however, has focused on the catalytic properties and how these are related to the local environment of titanium [61–63].

Pickup and co-workers [57,58] have used Ti isotopic substitution on GEM to perform a comprehensive study of the titanium environment in these materials, yielding a wealth of information, and only a part of the work can be described here. Titania–silica sol–gel samples were made, containing natural Ti, ^{46}Ti and ^{48}Ti. Taking into account the less than complete degree of enrichment, each of these has a different coherent neutron scattering length, as follows: ^{nat}Ti, $\bar{b} = -3.438$ fm; ^{46}Ti, $\bar{b} = 2.469$ fm; and ^{48}Ti, $\bar{b} = -6.063$ fm. This is the essence of the isotopic substitution method—if two experiments are performed where the coherent neutron scattering length of element A is changed from $\bar{b}_{A1}$ to $\bar{b}_{A2}$ by isotopic substitution then, following from Eq. (5), the difference between the experimental correlation functions is

$$\Delta T(r) = T_1(r) - T_2(r) = c_A((\bar{b}_{A1})^2 - (\bar{b}_{A2})^2)t_{AA}(r) + 2c_A(\bar{b}_{A1} - \bar{b}_{A2})\sum_{j \neq A} \bar{b}_j t_{Aj}(r). \quad (9)$$

Thus, the difference function contains information only on the A–X correlations which involve element A and any second element X, and this can be much more readily interpreted than the full correlation function, $T(r)$, which depends on the correlations between $N(N+1)/2$ different pairs of elements.

In addition to the requirement for detector stability, it is necessary that the samples are identical, apart from their isotopic compositions. Hence, great care was taken to ensure reproducibility of the complex sol–gel sample preparation [64], and subsequently the samples were checked to be identical by several methods including X-ray diffraction and elemental analysis. The final stage of sample manufacture was calcination at temperatures of 250, 500 and then 750 °C. As is consistent with the sol–gel preparation method, the samples contained significant residual –OH (about 20 atom% hydrogen after calcination at 250 °C, and about 10 atom% hydrogen after calcination at both higher temperatures). The incoherent scattering from the hydrogen in the samples was removed from the neutron diffraction data using the procedure described by Yang et al.

[18]. Three sets of sol–gel samples were made with nominal TiO_2–SiO_2 compositions (i.e. neglecting the H_2O content) of 8, 18 and 41 mol% TiO_2.

The interpretation for this study focuses naturally on the isotope difference observed in real-space, after Fourier transformation of the data, since this yields a clear separation of the Ti–O correlations, as is shown below. However, this difference is directly observed in reciprocal-space, and as an example Fig. 8 shows how the difference, i_{Ti-X} (Q), between the distinct scattering for the ^{46}Ti-enriched and ^{48}Ti-enriched 18 mol% TiO_2 samples, calcined at 750 °C, arises. A clear difference is observed in the distinct scattering, depending on the titanium isotope, and this difference depends only on Ti–X correlations (where X is any second element, Ti, O or Si).

Fig. 9 shows the total correlation function, $T(r)$, measured for the ^{46}Ti-enriched and ^{48}Ti-enriched 18 mol% TiO_2 samples, calcined at 750 °C, together with their difference, $\Delta T(r)$. The total correlation function peaks at ~1.6, ~2.6 and ~3 Å are due respectively to Si–O, O–O and Si–Si distances. The information on Ti–O distances is contained in the weak features between 1.75 and 2.10 Å, negative for the ^{48}Ti enriched sample and positive for the ^{46}Ti enriched sample. The large difference in the neutron scattering lengths of these two isotopes leads to a clearly visible peak in the difference correlation function, and it is only by isotopic substitution that these features can be isolated, so that accurate information on the Ti environment can be obtained. The difference correlation function, $\Delta T(r)$, shows that there are two different Ti–O distances of 1.81 and 1.95 Å, with the latter seen as a distinct, partially resolved shoulder. This is the first direct, unequivocal observation of two Ti–O distances in this type of material. The shorter Ti–O distance is due to titanium tetrahedrally substituted within the silica network, whilst the longer Ti–O distance is due to a minority of titanium which are in TiO_6 octahedral sites, similar to those in the mineral anatase (TiO_2), and at least some of the octahedrally coordinated Ti is in the form of phase-separated crystalline anatase. Table 3 gives the parameters from fitting the Ti–O peak in $\Delta T(r)$ for all of the samples studied.

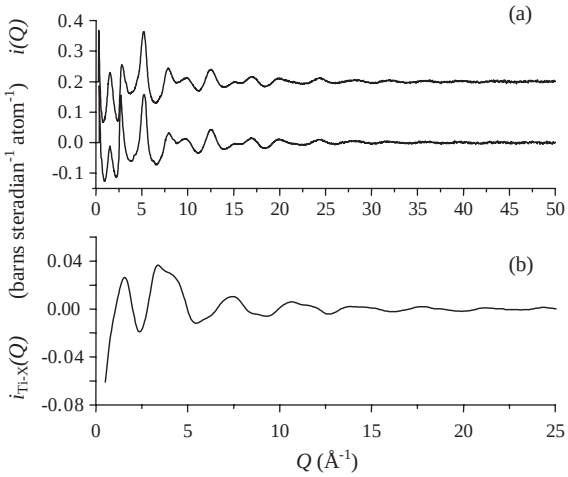

Fig. 8. (a) The distinct scattering, $i(Q)$, for the ^{46}Ti-enriched (upper trace, displaced vertically by 0.2 units) and ^{48}Ti-enriched (lower trace) 18 mol% TiO_2 samples, calcined at 750 °C, and b) the difference, i_{Ti-X} (Q), between these two data sets, which depends only on Ti–X correlations.

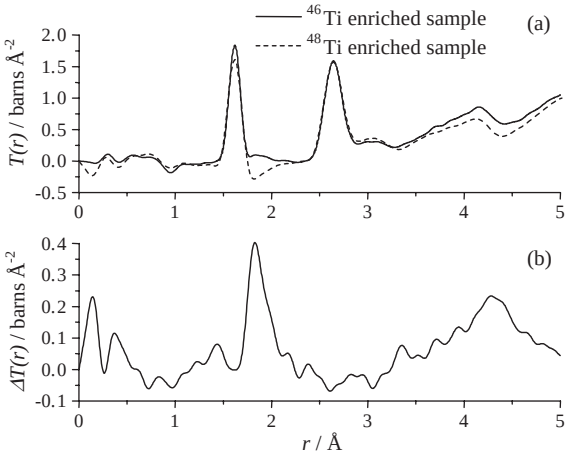

Fig. 9. (a) The total correlation functions, $T(r)$, for the ^{46}Ti-enriched and ^{48}Ti-enriched 18 mol% TiO_2 samples, calcined at 750 °C, and b) the difference correlation function, $\Delta T(r)$, which depends only on Ti–X correlations.

Fig. 10 shows the difference correlation function, $\Delta T(r)$, for the sample with 18 mol% TiO_2, measured for a sequence of calcination temperatures. This shows the evolution of the titanium coordination with calcination temperature. After calcination at 250 °C, the Ti occupies a distorted octahedral environment similar to that in the

Table 3
Details of the titanium–oxygen correlations (bond lengths, r_{TiO}, coordination numbers, n_{TiO}, and variation in distance, σ_{TiO}) from fitting the isotopic substitution data for titanium silicate sol–gel materials [58]

Nominal Composition (mol% TiO_2)	Calcination Temperature (°C)	r_{TiO} (Å) ± 0.01 Å	n_{TiO} ± 20%	σ_{TiO} (Å) ± 0.01 Å
8	250	1.84	3.3	0.04
		2.01	1.7	0.03
8	500	1.82	3.7	0.05
8	750	1.83	3.6	0.04
18	250	1.89	3.6	0.08
		2.11	1.5	0.05
18	500	1.84	3	0.06
		2.02	1.4	0.06
18	750	1.81	2.4	0.03
		1.95	1.7	0.06
41	500	1.82	0.9	0.05
		1.95	2.9	0.11

mineral ramsayite ($Na_2O \cdot 2TiO_2 \cdot 2SiO_2$), with four Ti–O bond lengths of 1.89 Å and two more Ti–O bond lengths close to 2.11 Å. After calcination at 500 °C, two Ti–O distances of 1.84 and 2.10 Å are observed, consistent with the presence of both distorted octahedral titanium, and titanium which are tetrahedrally substituted within the silica network.

For the sample with 8 mol% TiO_2, the titanium environment undergoes a rather different evolution. After calcination at 250 °C, two Ti–O distances are observed, one at 1.84 Å due to tetrahedrally substituted titanium, and one at 2.01 Å due to six coordinated titanium. However, heating this sample to higher temperatures (500 and 750 °C) converts all of the TiO_6 sites to TiO_4. It is perhaps surprising that essentially the same result has been found for a titanium silicate glass of similar composition, made by a very different preparation route; Corning ULE (ultra low expansion) glass, which contains 5.7 mol% TiO_2, is manufactured by a flame hydrolysis process which employs mixed silicon and titanium tetrachloride vapours in a gas-oxygen burner at greater than 1700 °C. Combustion reactions form submicron-sized molten titanium silicate particles which are collected and fused into a large solid boule of glass. Stone et al. [65] have found that in ULE glass the titanium are all coordinated by four oxygens, so that it is simply substituting for silicon in the vitreous network.

The neutron diffraction results on the sample with 41 mol% TiO_2 were less extensive, because phase separation and crystallisation effects were much more severe for this composition.

7. The structures of the disordered crystalline cyanides, CuCN, AgCN and AuCN

As well as being ideally suited to correlation function studies of non-crystalline materials (see previous sections), GEM is an excellent diffractometer for the study of crystalline powders [3–6]. In combination, these two capabilities make GEM a very powerful instrument for the study of disorder in crystalline materials.

The correlation function approach to the structure of non-crystalline materials has been in use for a number of decades, ever since the pioneering work of Warren [66], but has only recently begun to be applied widely to the study of crystalline materials, especially those with a disordered structure [67,68]. GEM is ideally suited to such studies of the structure of disordered crystals, as is demonstrated by recent work on group 11 cyanide crystals. The conventional approach to the study of the structure of crystalline materials by diffraction makes use of the Bragg peaks, and for powder samples the data are usually analysed by Rietveld refinement. This approach yields information on the average

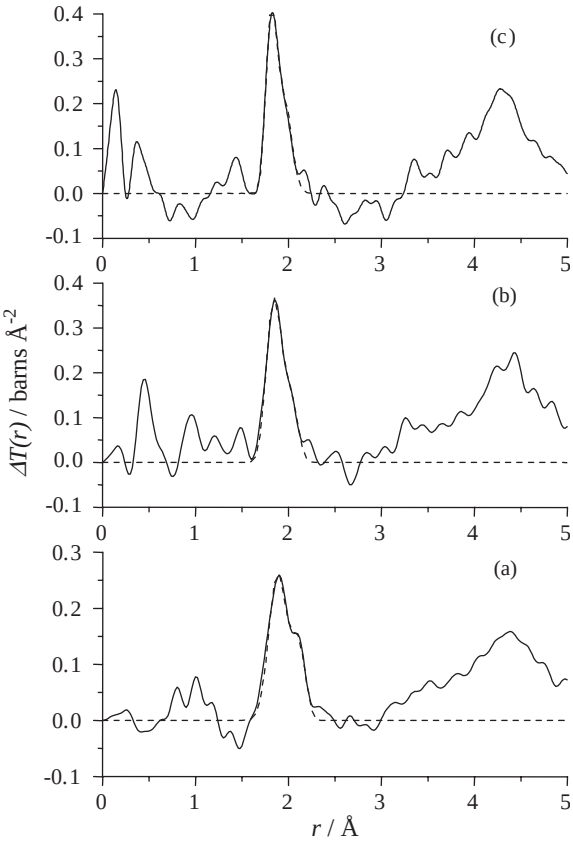

Fig. 10. The difference correlation function, $\Delta T(r)$, for the 18 mol% TiO_2 sample, heated to (a) 250 °C, (b) 500 °C and (c) 750 °C. The continuous lines show the experimental results, and the dashed lines show fits to the Ti–O correlation.

structure, since it assumes that every unit cell of the crystal is the same. By contrast, the correlation function yields direct information on the local structure of the crystal which, for disordered systems, is not the same as the average structure. Thus the combined use of Rietveld refinement and correlation function studies can be a very powerful means of elucidating the structure of disordered crystals [69].

For such apparently simple systems, definitive structures of the group 11 cyanides, MCN (where M is Cu, Ag or Au) have proved remarkably elusive. There has been a number of earlier studies of the structures of these compounds, but the most significant was the neutron Bragg diffraction study

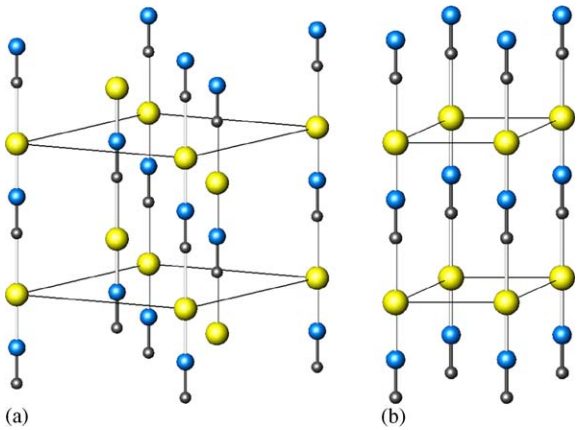

Fig. 11. The crystal structures of (a) AgCN and (b) AuCN, according to Bowmaker et al. [70]. The metal ions are shown with the largest radius, and the carbons are shown with the smallest radius. The unit cell is shown by thin lines, and the *c*-axis runs from top to bottom. The cyanide bonds are darkly shaded.

reported by Bowmaker et al. [70], who determined the structures for AgCN and AuCN shown in Fig. 11, but were unable to determine the structure of CuCN. The common feature of these crystals is that they involve infinite linear –M–(C≡N)–M–(C≡N)– chains, which run parallel to the *c*-axis. In the case of AuCN the gold atoms are in layers, due to an aurophilic interaction, whereas in AgCN the silver atoms in neighbouring chains are displaced along the chain axis by one third of the chain repeat distance.

GEM was used to perform neutron diffraction on samples of all three group 11 cyanides, at temperatures of both 300 and 10 K [67,71–74]. Fig. 12 shows the interference function, $Qi(Q)$, of the three samples at 300 K, all of which consist of sharp Bragg peaks for Q below about 10 $Å^{-1}$, together with an unusual sawtooth-like diffuse signal. The crystal structure of CuCN was solved for the first time, by noting the similarities between the CuCN and AgCN diffraction patterns, and subsequently refined by performing Rietveld refinement of the GEM data [72], as shown in Fig. 13, which showed that CuCN is isomorphous with AgCN. Nevertheless there were some small unexplained peaks in the diffraction pattern, which were ascribed to the presence of a minority

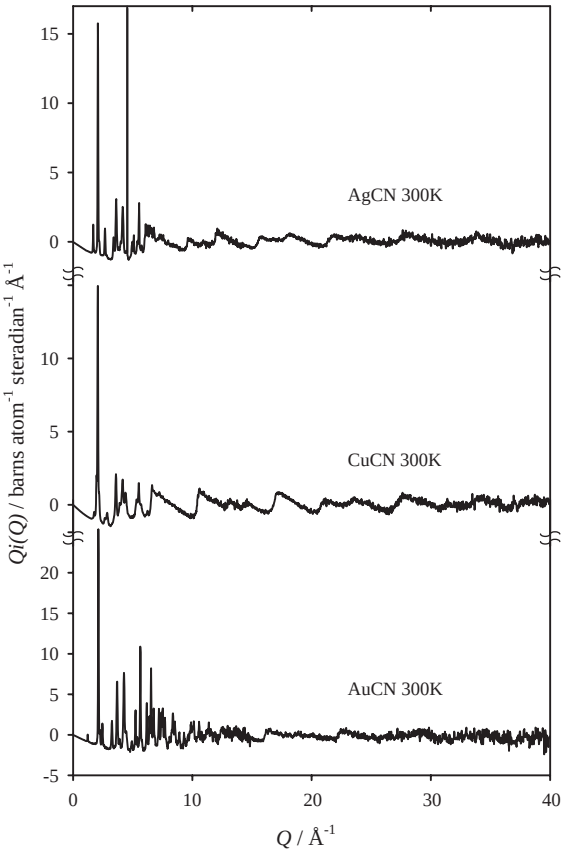

Fig. 12. The interference function, $Qi(Q)$, at 300 K for AgCN (top), CuCN (middle) and AuCN (bottom).

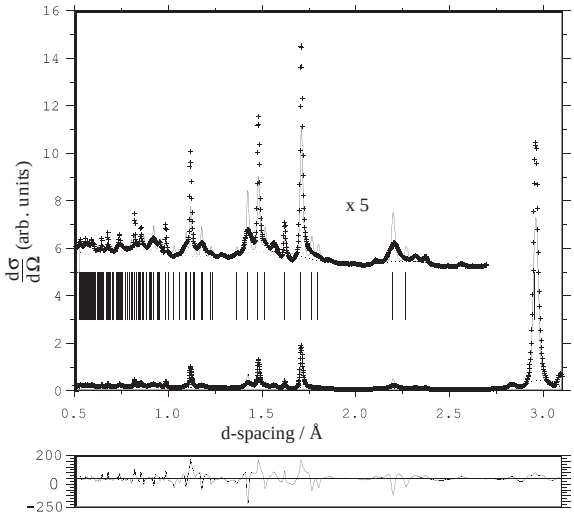

Fig. 13. Final fitted profiles (crosses, observed; line, calculated) from Rietveld refinement for CuCN at 10 K shown in upper frame. Vertical tick lines indicate the positions of the allowed reflections. The lower frame shows the residuals (I_{Iobs}–I_{calc})/ e.s.d. for the fit.

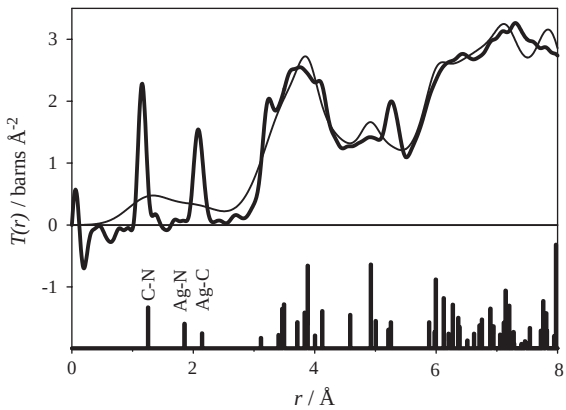

Fig. 14. The total correlation function, $T(r)$, for AgCN at 300 K (bold line), compared with the correlation function calculated according to Bowmaker et al.'s [70] crystal structure (light line), including the broadening effects of thermal motion and real-space resolution. The lower frame shows the correlation function (in arbitrary units) for Bowmaker et al.'s crystal structure without broadening.

phase of CuCN. Wang et al. [75] then showed that there are low temperature (LT) and high temperature (HT) forms of CuCN, and that the LT polymorph transforms irreversibly into the HT polymorph; the sample studied on GEM was mostly HT-CuCN, but contained a small fraction of LT-CuCN. In performing Rietveld refinement of the data for CuCN, AgCN and AuCN, it was found that, if anisotropic thermal parameters were used, then they did not behave reasonably, and had a tendency to become very large along the direction of the chains, giving some indication of the nature of the disorder in these materials.

The diffraction data for a crystalline sample, when Fourier transformed according to Eq. (3), yield a correlation function, $T(r)$, in the same way as for a glass. Fig. 14 shows $T(r)$ for AgCN at 300 K, the first peak of which, at about 1.16 Å, is due to the C–N bond length. It is apparent from the single sharp peak at about 2.08 Å that, within the limits of detection, the Ag–C and Ag–N bonds have the same length. Similarly, as shown in Table 4, the M–C and M–N bond lengths have

Table 4
M–C/N bond lengths at room temperature for group 11 cyanides [74]

Sample	M–C/N distances from previous Rietveld study [70] (Å)	M–C/N distance from $T(r)$ (Å)
CuCN	—	$r_{Cu-C} = r_{Cu-N} = 1.8538(1)$
AgCN	$r_{Ag-C} = 2.15(6)$, $r_{Ag-N} = 1.86(8)$	$r_{Ag-C} = r_{Ag-N} = 2.0850(4)$
AuCN	$r_{Au-C} = 2.06(2)$, $r_{Au-N} = 1.82(2)$	$r_{Au-C} = r_{Au-N} = 1.9703(5)$

been found to be identical (or very similar) in both CuCN and AuCN. This result contradicts the previous neutron Bragg diffraction study [70], which gave significantly different lengths for the two bonds in both AgCN and AuCN. However, it is the correlation function result which is correct, because $T(r)$ is an entirely model-independent probe of the local structure, whereas the results from Rietveld refinement depend upon a model, due to the necessity of specifying a space group and the implicit assumption that all unit cells are the same. It may seem surprising that the M–C and M–N bond lengths are the same in these cyanides, but this result is consistent with magnetic resonance studies of AgCN [76] and CuCN [77] which show head–tail disorder of the cyanide groups. (Unfortunately, a consequence of the great similarity of the M–C and M–N bond lengths is that the correlation function has a very low sensitivity to the presence of head-tail disorder.) Furthermore, quantum mechanical calculations of the properties of M–CN and M–NC monomers show very small differences between the M–C and M–N bond lengths (where M is Cu, Ag or Au) [78].

The correlation function for Bowmaker et al.'s [70] crystal structure of AgCN at 300 K was calculated using the XTAL program [79]. The lower part of Fig. 14 shows the correlation function for this crystal structure, without the broadening effects of resolution and thermal motion, and the difference between the Ag–N and Ag–C bond lengths is clearly apparent. In the upper part of Fig. 14 the crystal correlation function has been broadened using the temperature factors reported by Bowmaker et al. [70], and also for the effects of real-space resolution arising from the finite Q_{max} and the use of the Lorch modification function. It is clear that the thermal parameters from the Rietveld refinement lead to

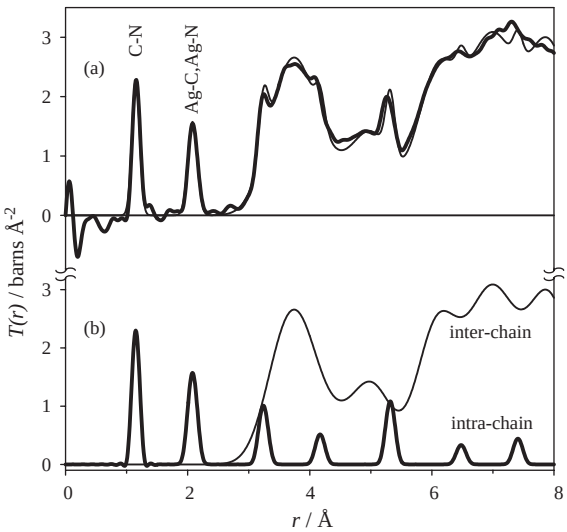

Fig. 15. (a) The total correlation function, $T(r)$, for AgCN at 300 K (bold line), compared with the correlation function for the random chain displacement model (light line), and (b) the intra-chain (bold line) and inter-chain (light line) components of the correlation function for the random chain displacement model.

gross over-estimates of the widths of the peaks in the correlation function. Detailed inspection of the experimental correlation function shows that the peaks which arise from inter-chain correlations are much broader than the peaks which arise from intra-chain correlations. This leads to a random chain displacement model, in which the interatomic distances within a chain are well-defined, but the chains are subject to random displacements along the c-axis relative to each other. Fig. 15 shows a comparison between the experimental correlation function and the correlation function calculated according to the random chain displacement model, which gives much better agreement than the model based on Rietveld refinement results shown in Fig. 14. The intra-chain compo-

nent of the model correlation function was broadened using a RMS variation in interatomic distance of 0.0595 Å (except for the C≡N bond in the cyanide group, for which a value 0.0358 Å was used). A much larger RMS variation of 0.2964 Å was used to broaden the inter-chain component of the model correlation function. This larger peak width incorporates a large contribution from static disorder, in addition to the contribution from thermal motion, and it arises as a result of the relatively weak van der Waals bonding between the chains. The random chain displacement disorder is found to be greatest in CuCN and least in AuCN (due to the aurophilic bonding), and this helps to explain why Bragg diffraction data for CuCN are the most difficult to refine [70].

The random chain displacement model leads to an understanding of the sawtooth diffuse scattering observed in the interference functions shown in Fig. 12; the sawtooth is most apparent for higher values of Q, in which region only interatomic correlations with a small variation in interatomic distance are of significance, and therefore the sawtooth arises from intra-chain correlations. The sawtooth is the diffraction pattern of a one-dimensional crystal, and this diffuse scattering waveform is a unique signature in the diffraction pattern for ordered one-dimensional structures.

Table 5 gives the change with temperature of the c lattice parameter and the inter-chain distance, as calculated directly from the a lattice parameter, both of which were derived by Rietveld refinement of the diffraction data. Most notably there is a small negative thermal expansion (NTE) along the c-axis. Table 5 also gives the change with temperature of the chain repeat distance, calculated by a suitable sum of the distances derived from the positions of the peaks in the correlation function ($r_{C-N}+2r_{M-C/N}$). It is found that generally the chain repeat distance does not show the same NTE, and that the chain repeat distance is longer than the c-axis of the crystal cell. This behaviour reveals the nature of the dominant vibrational motions of the chains. These motions involve long wavelength cooperative motions of relatively large numbers of atoms in a direction perpendicular to the c direction. The displacements for these modes are relatively large due to the lack of strong bonding forces between the chains. A rise in temperature causes the population of these modes to increase so that there is an increase in the thermal atomic displacements perpendicular to the chain axis. The M–C/N and C≡N bonds are much stronger so that their length, and hence the overall length of the MCN chain, changes little with temperature. The transverse atomic displacements are compensated for by pulling the ends of the chain closer together, so that the chain length is preserved, and consequently there is a contraction of the c lattice parameter. These sideways motions of the atoms in the chains increase with temperature, resulting in a higher effective cross-section in the ab plane for each chain and, hence, expansion of the a lattice parameter with temperature. Supporting evidence for this interpretation was recently obtained when a single crystal of LT-CuCN was isolated and the structure was solved by single crystal X-ray diffraction [80]; there are infinite –M–(C≡N)– chains, as in HT-CuCN, but instead of being linear, they are arranged in a wave-like pattern.

Table 5
The change with temperature of key distances in the group 11 cyanides

Sample	CuCN	AgCN	AuCN			
Temperature (K)	10	300	10	300	10	300
c lattice parameter (Å)	4.86152(3)	4.82202(6)	5.28342(2)	5.26072(2)	5.08238(5)	5.07256(3)
% change in c		−0.8125		−0.4296		−0.1932
Inter-chain distance (Å)	3.413075	3.482092	3.409063	3.460638	3.3426(1)	3.3915(1)
% change in inter-chain distance		2.022		1.513		1.463
M–C–N–M distance from $T(r)$ (Å)	4.8493(2)	4.8650(2)	5.2910(2)	5.3288(12)	5.098(1)	5.090(1)

8. Conclusions

The recently constructed GEneral Materials diffractometer, GEM, at the ISIS Facility pulsed neutron source is the most advanced materials neutron diffractometer in the world. The excellent performance of GEM has been achieved by means of a highly stable detector array, which covers a very wide range in scattering angles and a very large solid angle, leading to a wide dynamic range and a high count rate. This enables GEM to attain high maximum momentum transfers, Q_{max}, in the region of 55 $Å^{-1}$ (depending on the order in the sample), as illustrated here by the splitting of P–O distances for bridging and non—bridging oxygens in bioactive phosphate glasses (which differ by approximately 0.12 Å). Experimental data for deuterated amorphous silicon show how the novel low angle detector bank, Bank0, allows GEM to reach low momentum transfers of order 0.1 $Å^{-1}$. GEM has been used to perform the first successful isotopic substitution experiment on sol–gel materials in a study of amorphous titanium silicates, showing the suitability of the instrument for both isotopic substitution, and for studies of complex materials, even in the presence of hydrogen. Studies of the disordered crystalline group 11 cyanides show the great power of GEM to investigate disorder in crystals by the combined use of crystallographic and correlation function methods. The crystal structure of high temperature CuCN has been determined, and it is found to be isomorphous with AgCN. The disorder in AuCN, AgCN and high temperature CuCN arises from relatively large static displacements of the linear –M–(C≡N)– chains (where M is Cu, Ag or Au) relative to each other. The one-dimensional NTE in the direction of the chain axis is due to long wavelength cooperative motions of the chains.

Acknowledgements

I am grateful to many people at ISIS, including all the members of the project engineering, detector, electronics, and user support groups. Without the exertions of these groups, GEM would not have been designed and constructed so well, and the data shown here could not have been collected. I am grateful to Isaac Abrahams and Tiziana di Cristina (Queen Mary College, London University) for allowing me to make use of their data on phosphate glasses. Thanks are due to Adrian Wright (Reading University) for the loan of his silicon sample. Bob Newport and Dave Pickup (Kent University) are gratefully acknowledged for their help. Simon Hibble and Simon Cheyne (Reading University) are acknowledged for a stimulating collaboration on cyanides.

References

[1] W.G. Williams, R.M. Ibberson, P. Day, J.E. Enderby, Physica B 241–243 (1998) 234.
[2] A.C. Hannon, in: J. Lindon, G. Tranter, J. Holmes (Eds.), Encyclopedia of Spectroscopy and Spectrometry, vol. 2, Academic Press, London, 2000, p. 1479.
[3] P. Day, J.E. Enderby, W.G. Williams, L.C. Chapon, A.C. Hannon, P.G. Radaelli, A.K. Soper, Neutron News 15 (2004) 19.
[4] P.G. Radaelli, A.C. Hannon, L.C. Chapon, Notiz. Neut. Luce. Sinc. 8 (2003) 19.
[5] P. Day, Chem. Br. 36 (2000) 24.
[6] P. Day, Mater. World 8 (2000) 25.
[7] J.C. Wasse, S. Hayama, S. Masmanidis, S.L. Stebbings, N.T. Skipper, J. Chem. Phys. 118 (2003) 7486.
[8] U. Hoppe, E. Yousef, C. Rüssel, J. Neuefeind, A.C. Hannon, Solid State Commun. 123 (2002) 273.
[9] U. Hoppe, E. Yousef, C. Rüssel, J. Neuefeind, A.C. Hannon, J. Phys.: Condens. Matter 16 (2004) 1645.
[10] U. Hoppe, I. Gugov, H. Bürger, P. Jóvári, A.C. Hannon, J. Phys.: Condens. Matter 17 (2005) 2365.
[11] G. Walter, U. Hoppe, J. Vogel, G. Carl, P. Hartmann, J. Non-Cryst. Solids 333 (2004) 252.
[12] U. Hoppe, G. Walter, G. Carl, J. Neuefeind, A.C. Hannon, J. Non-Cryst. Solids 351 (2005) 1020.
[13] J.M. Cole, A.C. Hannon, R.A. Martin, R.J. Newport, Phys. Rev. Lett. (2005) submitted.
[14] U. Hoppe, R. Kranold, J.M. Lewis, C.P.O. Brien, H. Feller, S. Feller, M. Affatigato, J. Neuefeind, A.C. Hannon, Phys. Chem. Glasses 44 (2003) 272.
[15] H. Brequel, S. Enzo, F. Babonneau, P.G. Radaelli, Mater. Sci. Forum 386–388 (2002) 275.
[16] H. Brequel, S. Enzo, S. Walter, G.D. Sorarù, R. Badheka, F. Babonneau, Mater. Sci. Forum 386–388 (2002) 359.
[17] H. Brequel, S. Enzo, G. Gregori, H.-J. Kleebe, A.C. Hannon, Mater. Sci. Forum 386–388 (2002) 365.
[18] H. Yang, R.I. Walton, S. Antonijevic, S. Wimperis, A.C. Hannon, J. Phys. Chem. B 108 (2004) 8208.
[19] A. Szczygielska, A. Burian, J.C. Dore, S. Duber, A.C. Hannon, Proc. SPIE 5136 (2003) 288.

[20] A. Burian, J. Koloczek, J.C. Dore, A.C. Hannon, J.B. Nagy, A. Fonseca, Diamond Relat. Mater. 13 (2003) 1261.
[21] J. Koloczek, A. Burian, J.C. Dore, A.C. Hannon, Diamond Relat. Mater. 13 (2003) 1218.
[22] P.F. Peterson, T. Proffen, I.K. Jeong, S.J.L. Billinge, K.S. Choi, M.G. Kanatzidis, P.G. Radaelli, Phys. Rev. B 6316 (2001) 165211.
[23] M.G. Tucker, M.T. Dove, D.A. Keen, J. Appl. Crystallogr. 34 (2001) 780.
[24] M.T. Dove, M.G. Tucker, D.A. Keen, Eur. J. Min. 14 (2002) 331.
[25] M.T. Dove, Eur. J. Min. 14 (2002) 203.
[26] J. Haines, O. Cambon, D.A. Keen, Physica B 350 (2004) e979.
[27] P. Gorria, L. Fernandez Barquin, V.M. Prida, W.S. Howells, J. Magn. Magn. Mater. 254–255 (2003) 504.
[28] M. Al-Jawad, S.H. Kilcoyne, P. Manuel, Phys. Chem. Glasses 45 (2004) 97.
[29] A.C. Hannon, in: J. Lindon, G. Tranter, J. Holmes (Eds.), Encyclopedia of Spectroscopy and Spectrometry, vol. 2, Academic Press, London, 2000, p. 1493.
[30] A.C. Wright, J. Non-Cryst. Solids 76 (1985) 187.
[31] M.A. Howe, R.L. McGreevy, W.S. Howells, J. Phys.: Condens. Matter 1 (1989) 3433.
[32] R.N. Sinclair, A.C. Wright, Nucl. Instr. and Meth. 114 (1974) 451.
[33] G. Placzek, Phys. Rev. 86 (1952) 377.
[34] E. Lorch, J. Phys. C 2 (1969) 229.
[35] W.S. Howells, A.C. Hannon, J. Phys.: Condens. Matter 11 (1999) 9127.
[36] A.C. Hannon, J. Phys.: Condens. Matter 11 (47) (1999).
[37] D.I. Grimley, A.C. Wright, R.N. Sinclair, J. Non-Cryst. Solids 119 (1990) 49.
[38] J.F. Bent, Ph.D. Thesis, University of Warwick, England, 1999.
[39] A.F. Wright, M. Berneron, S.P. Heathman, Nucl. Instr. ans Meth. 180 (1981) 655.
[40] N.J. Rhodes, M.W. Johnson, E.M. Schooneveld, in: S. Itoh, J. Suzuki (Eds.), ICANS-XV 15th Meeting of the International Collaboration on Advanced Neutron Sources, vol. 1, JAERI, Tokaimura, Tsukuba, Japan, 2000, p. 646.
[41] P.A.V. Johnson, A.C. Wright, R.N. Sinclair, J. Non-Cryst. Solids 58 (1983) 109.
[42] M. Vallet-Regi, J. Chem. Soc. Dalton Trans. (2001) 97.
[43] H.M. Kim, J. Ceram. Soc. Japan 109 (2001) S49.
[44] T. di Cristina, Ph.D. Thesis, Queen Mary College, University of London, England, 2004.
[45] I. Abrahams, T. di Cristina, A.C. Hannon, 2004, in preparation.
[46] S.F. Mughabghab, M. Divadeenam, N.E. Holden, Neutron Cross Sections. Neutron Resonance Parameters and Thermal Cross Sections. Part A, $Z = 1$–60, vol. 1, Academic Press, New York, 1981.
[47] A.K. Soper, P. Buchanan, private communication, 2004.
[48] A.C. Hannon, 2004, http://www.isis.rl.ac.uk/disordered/Manuals/gudrun/gudrun_GEM.htm
[49] A.C. Hannon, W.S. Howells, A.K. Soper, IOP Conf. Ser. 107 (1990) 193.
[50] A.C. Hannon, D.I. Grimley, R.A. Hulme, A.C. Wright, R.N. Sinclair, J. Non-Cryst. Solids 177 (1994) 299.
[51] K. Suzuki, M. Ueno, J. Phys. Colloque 8 (Suppl. 46) (1985) 261.
[52] U. Hoppe, G. Walter, R. Kranold, D. Stachel, J. Non-Cryst. Solids 263–264 (2000) 29.
[53] C.G. Windsor, R.N. Sinclair, Nucl. Instr. and Meth. A 242 (1986) 185.
[54] G. Porod, Kolloid Z. Z. Polym. 124 (1951) 83.
[55] C.A. Guy, A.C. Wright, R.N. Sinclair, R.J. Stewart, F. Jansen, J. Non-Cryst. Solids 196 (1996) 260.
[56] A.C. Wright, T.M. Brunier, C.A. Guy, R.N. Sinclair, A.C. Hannon, F. Jansen, Physica A 201 (1993) 395.
[57] D.M. Pickup, F.E. Sowrey, K.O. Drake, M.E. Smith, R.J. Newport, Chem. Phys. Lett. 392 (2004) 503.
[58] D.M. Pickup, F.E. Sowrey, R.J. Newport, P.N. Gunawidjaja, K.O. Drake, M.E. Smith, J. Phys. Chem. B 108 (2004) 10872.
[59] C.J. Brinker, G.W. Scherer, Sol–Gel Science: The Physics and Chemistry of Sol–Gel Processing, Academic, San Diego, 1990.
[60] P.C. Schultz, H.T. Smyth, in: R.W. Douglas, B. Ellis (Eds.), Amorphous Materials, Wiley, London, 1970, p. 453.
[61] R.J. Davis, Z. Liu, Chem. Mater. 9 (1997) 2311.
[62] S. Inamura, T. Nakai, H. Kanai, T. Ito, Faraday Trans. 91 (1995) 1261.
[63] C. Beck, T. Mallat, T. Bürgi, A. Baiker, J. Catal. 204 (2001) 428.
[64] M.A. Holland, D.M. Pickup, G. Mountjoy, S.C.E. Tsang, G.W. Wallidge, M.E. Smith, R.J. Newport, J. Mater. Chem. 10 (2000) 2495.
[65] C.E. Stone, A.C. Wright, R.N. Sinclair, A.C. Hannon, A. Musinu, T.P. Seward III, H.A. Feller, Phys. Chem. Glasses 43C (2002) 63.
[66] B.E. Warren, H. Krutter, O. Morningstar, J. Am. Ceram. Soc. 19 (1936) 202.
[67] S.J. Hibble, A.C. Hannon, in: S.J.L. Billinge, M.F. Thorpe (Eds.), From Semiconductors to Proteins: Beyond the Average Structure, Kluwer Academic/Plenum Publishers, New York, 2002, p. 129.
[68] S.J.L. Billinge, M.G. Kanatzidis, Chem. Commun. (2004) 749.
[69] S.J. Hibble, A.C. Hannon, I.D. Fawcett, J. Phys.: Condens. Matter 11 (1999) 9203.
[70] G.A. Bowmaker, B.J. Kennedy, J.C. Reid, Inorg. Chem. 37 (1998) 3968.
[71] S.J. Hibble, S.M. Cheyne, A.C. Hannon, S.G. Eversfield, Inorg. Chem. 41 (2002) 1042.
[72] S.J. Hibble, S.M. Cheyne, A.C. Hannon, S.G. Eversfield, Inorg. Chem. 41 (2002) 4990.
[73] S.J. Hibble, A.C. Hannon, S.M. Cheyne, Inorg. Chem. 42 (2003) 4724.
[74] S.M. Cheyne, Ph.D. Thesis, University of Reading, England, 2004.

[75] J. Wang, M.F. Collins, G.P. Johari, Phys. Rev. B 65 (2002) 180103(R).
[76] D.L. Bryce, R.E. Wasylishen, Inorg. Chem. 41 (2002) 4131.
[77] S. Kroeker, R.E. Wasylishen, J.V. Hanna, J. Am. Chem. Soc. 121 (1999) 1582.
[78] O. Dietz, V.M. Rayón, G. Frenking, Inorg. Chem. 42 (2003) 4977.
[79] A.C. Hannon, Rutherford Appleton Laboratory Report RAL-93-063, 1993.
[80] S.J. Hibble, S.G. Eversfield, A.R. Cowley, A.M. Chippindale, Angew. Chem. -Int. Ed. 43 (2004) 628.